LETTER

doi:10.1038/nature14103

Orientation columns in the mouse superior colliculus

Evan H. Feinberg[1] & Markus Meister[1,2]

More than twenty types of retinal ganglion cells conduct visual information from the eye to the rest of the brain[1,2]. Each retinal ganglion cell type tessellates the retina in a regular mosaic, so that every point in visual space is processed for visual primitives such as contrast and motion[3]. This information flows to two principal brain centres: the visual cortex and the superior colliculus. The superior colliculus plays an evolutionarily conserved role in visual behaviours[4], but its functional architecture is poorly understood. Here we report on population recordings of visual responses from neurons in the mouse superior colliculus. Many neurons respond preferentially to lines of a certain orientation or movement axis. We show that cells with similar orientation preferences form large patches that span the vertical thickness of the retinorecipient layers. This organization is strikingly different from the randomly interspersed orientation preferences in the mouse's visual cortex[5]; instead, it resembles the orientation columns observed in the visual cortices of large mammals[6–8]. Notably, adjacent superior colliculus orientation columns have only limited receptive field overlap. This is in contrast to the organization of visual cortex, where each point in the visual field activates neurons with all preferred orientations[9]. Instead, the superior colliculus favours specific contour orientations within ~30° regions of the visual field, a finding with implications for behavioural responses mediated by this brain centre.

We exposed the mouse superior colliculus (SC) for chronic brain imaging while leaving cortex intact (see Methods; Fig. 1a–c and Extended Data Fig. 1) and delivered the calcium indicator GCaMP6s as a neural activity reporter[10]. Awake mice head-fixed on a circular treadmill viewed stimuli on a tangent screen, while neuronal responses were monitored by two-photon microscopy (Fig. 1d). The focal plane of the microscope was roughly parallel to the surface of the SC and its retinotopic map of visual space[11,12]. The screen displayed thin bars drifting along their short axes (Fig. 1d), a stimulus that elicits orientation- or axis-tuned responses from many cells in the SC of anaesthetized mice, albeit by mechanisms that appear distinct from those of cortical neurons[13,14]. The animals remained stationary on most stimulus trials (72%, $n = 5$ animals, 208 stimulus blocks), and the fraction of stationary trials did not vary across visual stimuli ($P = 0.99$, Kruskal–Wallis test). Consequently, we report measurements from all trials regardless of locomotion; these results differ only subtly from those obtained by excluding running trials.

Neurons in the upper layers of the SC responded to drifting bars with large and reproducible transients in fluorescence that were often stronger to certain bar orientations than to others, consistent with previous reports of orientation tuning[14] (Fig. 1e, f). Unexpectedly, neighbouring neurons frequently displayed remarkably similar response profiles (Fig. 2a, b). Volumes of the SC (150 μm (anterior–posterior) × 280 μm (medial–lateral) × 40–80 μm (dorsal–ventral)) were analysed in several animals, with a focus on fields of view containing multiple groups of cells with different preferred orientations (Fig. 2c). The preferred orientations of orientation-selective cells separated horizontally by short distances (<100 μm) were much more alike than expected by chance (Fig. 2d and Extended Data Fig. 4a–c; mean $\Delta\theta \pm$ s.e.m., 28.6° ± 0.7; median $\Delta\theta$, 20.5° for 1,139 cell pairs), whereas preferred orientations of cells separated by greater distances (150–250 μm) were much less alike than expected by chance (Fig. 2d and Extended Data Fig. 4a–c; mean $\Delta\theta \pm$ s.e.m., 57.8° ± 1.2; median $\Delta\theta$, 63.6° for 440 cell pairs).

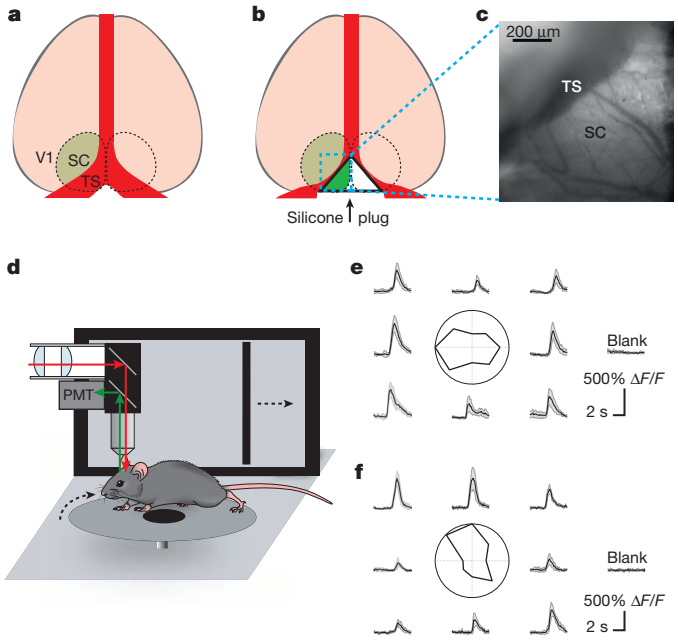

Figure 1 | Calcium imaging in awake mouse superior colliculus reveals orientation tuning. **a**, Schematic of mouse cerebral anatomy. The SC lies beneath visual cortex (V1) and the transverse sinus (TS). GCaMP6s-expressing SC is labelled in green. **b**, Schematic of cerebral anatomy after insertion of a triangular plug to reveal ~15–25% of the SC. **c**, Exposed portion of the SC. **d**, Schematic of experimental setup. Mice are head-fixed on a turntable and free to run. Visual stimuli are presented on a tangent screen while two-photon calcium imaging is used to record neural population activity. PMT, photomultiplier tube. **e**, **f**, Average fluorescence signal $\Delta F/F \pm$ s.d. of two SC neurons to 7 repetitions each of 8 directions of bar motion or a blank screen. Insets are polar plots of the peak responses.

[1]Center for Brain Science, Department of Molecular and Cellular Biology, Harvard University, 52 Oxford Street, Cambridge, Massachusetts 02138, USA. [2]Division of Biology and Biological Engineering, California Institute of Technology, Pasadena, California 91125, USA.

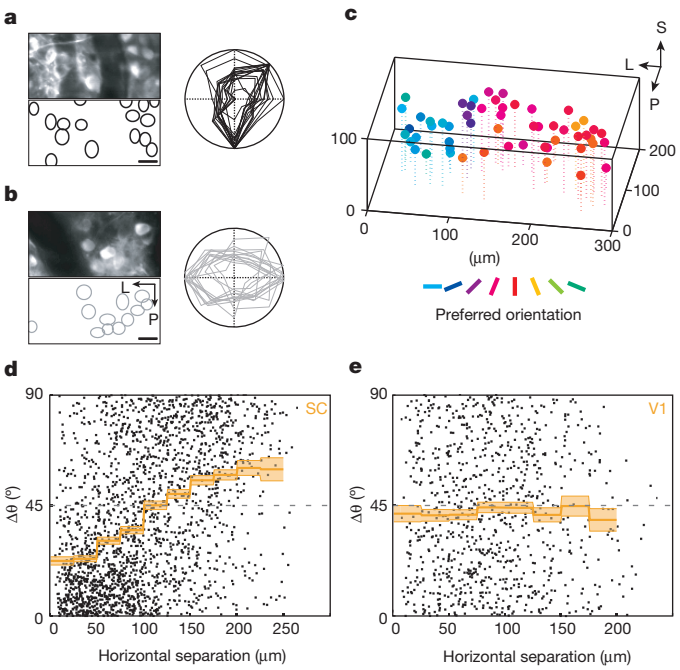

Figure 2 | Patches of neurons with similar orientation tuning in the superior colliculus. **a**, **b**, Two fields of cells in the SC (upper left panels) and corresponding elliptical regions of interest (lower left panels). Responses of the cells to drifting bars are overlaid in polar plots (right panels), normalized to peak responses. Scale bar, 20 μm. **c**, All orientation-tuned cells within a volume in the SC are plotted as spheres and colour-coded according to preferred orientations. L, lateral; P, posterior; S, superficial. **d**, **e**, Absolute value of the difference in preferred orientations plotted against horizontal distance in the SC (**d**) for 7 volumes in 6 animals ($n = 269$ cells, 2,077 pairs) and in V1 (**e**) for 3 volumes in 3 animals ($n = 104$ cells, 890 pairs). 0 and 90° correspond to identical and orthogonal orientation preferences, respectively, whereas 45° would be expected by chance (dashed grey line). Orange lines, means for 25-μm bins ± s.e.m.

These results were unexpected because the input to the SC from the retina is not thought to carry an orientation bias, even though individual retinal ganglion cells can be orientation-tuned[15]. We first considered the effects of optical projection from the flat tangent screen, which can alter the apparent width of a bar depending on its orientation, but the preferred orientations were not consistently biased towards or away from radial orientations (Extended Data Figs 1 and 2 and Supplementary Discussion). To confirm that the effects observed were not artefacts of our experimental system, we modified the surgical procedure to deliver GCaMP6s to both the SC and primary visual cortex (V1) and visualize both areas. Drifting bar stimuli elicited orientation-tuned responses from neurons in V1 (Extended Data Fig. 3) that were often sharper than in the SC[14,16] (mean orientation selectivity index (see Methods) of orientation-tuned neurons: 0.39 (V1) vs 0.31 (SC), $P = 0.003$), suggesting that surgical exposure of the SC spares V1 function. However, unlike in the SC, the arrangement of V1 neurons bore no relationship to their preferred orientation and was indistinguishable from chance[5]. (Fig. 2e and Extended Data Fig. 4d–f). Moreover, SC and V1 neurons had overlapping receptive fields, suggesting that the pattern observed in the SC is likely not inherited from the retina. This side-by-side comparison indicates that the orientation patches in the SC are not artefacts of the stimulus or imaging paradigms. Instead, the organization of orientation selectivity in the mouse SC differs substantially from that in visual cortex.

To probe the functional organization of the SC perpendicular to the brain surface we imaged neural responses at different depths. Pairs of neurons separated by <25 μm horizontally tended to share preferred orientations, regardless of depth separation, at least over 80 μm depth (Fig. 3a, b). In the deeper SC, fluorescence signals often became dimmer and less sharp, precluding efficient motion correction and accurate correction for neuropil contamination for single cells (Methods). Because SC cells and the surrounding neuropil are tuned alike (Extended Data Fig. 5), bulk fluorescence signals offer useful proxies for local orientation tuning that allowed analysis of deeper volumes (Fig. 3c). Orientation tuning was similar between slices of the same vertical column over depth separations up to 260 μm, but significantly different for slices drawn from different columns (Fig. 3d; $P < 0.001$, Kruskal–Wallis test). These results suggest that vertical columns of cells with similar orientation preferences span the retinorecipient SC (Fig. 3c, d).

To generate larger maps of orientation tuning in the SC, we turned to a complementary wide-field method: optical imaging of intrinsic signals[8]. Because most cells preferred orientations close to the cardinal axes (Extended Data Fig. 6), horizontal and vertical bars were used for intrinsic imaging experiments. Large patches (>200 μm diameter) of the SC preferred either horizontal or vertical bars (Fig. 4a). This arrangement was grossly reproducible across animals. The medial and lateral parts of the exposed SC, corresponding to the superior visual field and elevations close to the horizon, respectively, tended to prefer vertical bars—whereas the intervening area, which surveys intermediate elevations, tended to prefer horizontal bars (Fig. 4a–c). The orientation maps showed no relationship to the distortions introduced by the flat screen, and were robust to variations in the widths and velocities of the bars (Extended Data Fig. 7). These patches were reminiscent of the patterns observed in visual cortices of other mammalian species[7,8]. Attempts were made with limited success to aspirate the overlying cortex and blood vessels to expose more of the SC. In one instance, a small patch extending further anterior and lateral could be imaged, and the stereotyped orientation patches appeared in the expected locations.

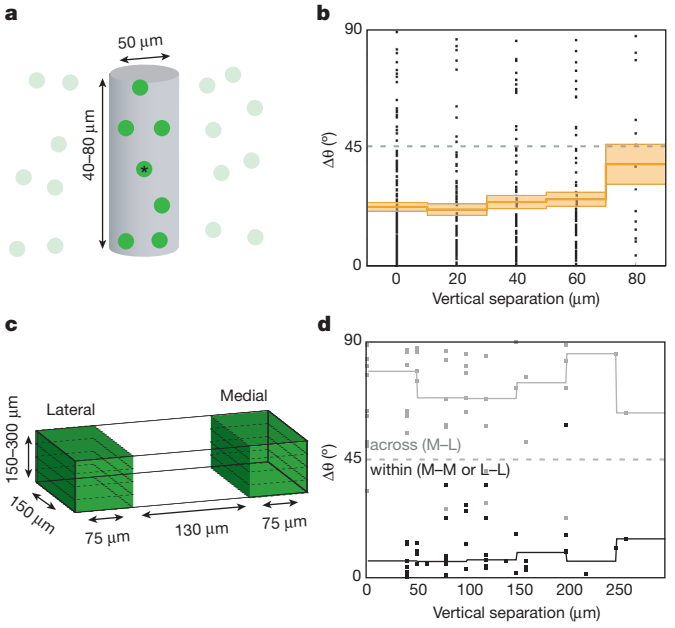

Figure 3 | Orientation patches form vertical columns. **a**, A cylinder centred on each neuron was projected through the volume and the similarity of its preferred orientation to that of each cell in the cylinder was determined. **b**, Difference in preferred orientations plotted against vertical distance. Orange lines, means for 20-μm bins ± s.e.m. Dashed grey line indicates chance. Differences across depths were not significant ($P > 0.1$, Kruskal–Wallis test; $n = 5$ animals, 397 pairs). **c**, Signals are averaged within 75 × 150 μm slices on the medial and lateral edges of an image plane, separated horizontally by 130 μm, at several depths along the vertical axis. **d**, Difference in preferred orientations plotted against vertical distance for orientation-tuned slices along the same vertical column (black dots) or adjacent vertical columns (grey dots). Lines indicate medians for 50-μm bins. M, medial slice; L, lateral slice. Data from 4 mice.

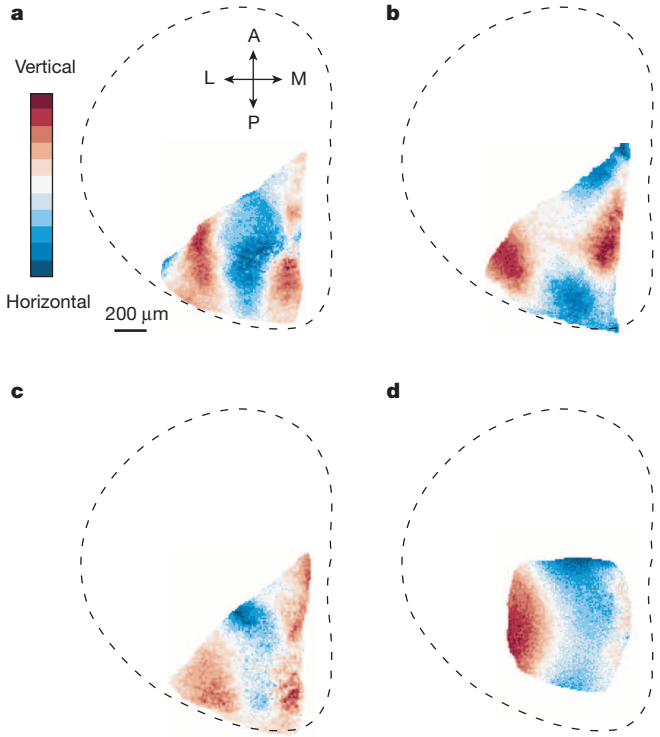

Figure 4 | Intrinsic imaging reveals larger orientation maps. **a**, Orientation map of the SC. Red areas respond more strongly to vertical bars and blue areas respond more strongly to horizontal bars. A, anterior; L, lateral; M, medial; P, posterior. The reflectance change $\Delta R/R$ from red to blue is 6×10^{-4} in **a** and **c**, 4×10^{-4} in **b** and 3×10^{-4} in **d**. The dashed outline indicates rough dimensions of the SC and approximate location of field of view. Midline blood vessels obscure the medial SC, containing cells with the most superior receptive fields. **b**, **c**, Orientation maps for two additional animals. **d**, Orientation map in an animal in which visual cortex and the transverse sinus had been surgically ablated weeks earlier. Granulation tissue over much of the SC limited the field of view.

This suggests that orientation columns in the SC arise even without input from the visual cortex (Fig. 4d).

These results indicate that cells in the SC with similar orientation preferences form patches within the retinotopic map of visual space, an arrangement that might preclude uniform coverage of different contour orientations throughout the visual field. This issue has been addressed in species with orientation columns in the visual cortex. There a uniform coverage is preserved because the grain of the orientation patches is so fine that any point in the visual field activates neurons of all possible orientation preferences[17–19]. To examine whether this applies in the mouse SC, we measured the projective fields on the SC for localized stimuli (Fig. 5a). Thin gratings produced activation stripes consistent with the known retinotopic map (Fig. 5b–d). Stripes had an average width of 170–190 μm (full-width at half-maximum, 4 stripes, 2 animals). Gratings separated by ~12° in space excited largely non-overlapping areas on the SC, with peak-to-peak distances of 100–170 μm ($n = 4$ pairs, 2 mice; Fig. 5b–d and Extended Data Figs 7 and 8). By comparison, the

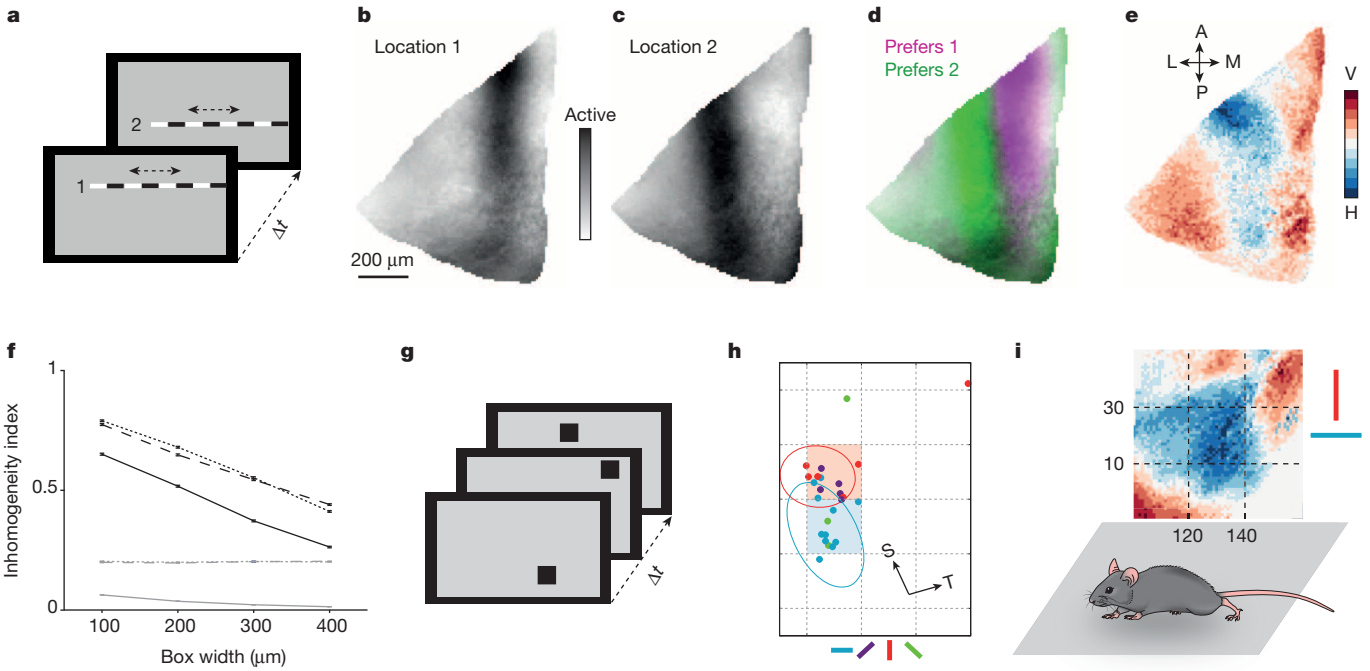

Figure 5 | Inhomogeneous coverage of contour orientation in the superior colliculus. **a**, Stimulus used to map retinotopy. **b**–**d**, Activation stripes elicited by the grating slit presented at positions 1 and 2 from **a**. Darker areas are more strongly activated. The reflectance change $\Delta R/R$ from black to white is 2×10^{-3} in both panels. **e**, Orientation map (from Fig. 4c). V, vertical; H, horizontal. **f**, Inhomogeneity indices for 3 mice from Fig. 4a–c for sampling windows 100–400 μm wide. Each black line corresponds to one mouse; each grey line corresponds to data from a shuffled orientation map. Error bars, s.e.m. **g**, Flashed spot stimulus used to map receptive fields in two-photon experiments. **h**, Receptive field centres (dots) for orientation-tuned cells in a field of view. Ellipses indicate two-dimensional Gaussian receptive field fits (radii 1 s.d.) for two representative cells. Image axes correspond to screen coordinates; dashed lines demarcate stimulus pixels. Red and blue squares indicate consensus receptive field centres of cells preferring vertical and horizontal bars, respectively. Arrows indicate projections of spherical coordinate axes from the animal's perspective. Arrow lengths, 5 degrees of visual angle. S, superior; T, temporal. **i**, Schematic of consequences of SC orientation columns for mouse vision. Image from Fig. 4a. In the temporal visual field, there are patches at high and low elevation where the SC prefers vertical bars and at intermediate elevation where it prefers horizontal bars. Approximate elevation and azimuth marked in degrees.

orientation patches spanned 200 μm to 400 μm in width (Fig. 5e; 3 animals), corresponding to ~30° of visual angle. Indeed, patches of the SC up to 300 μm wide were typically dominated by a particular preferred orientation (Fig. 5f). Thus the parcellation of orientation tuning is much coarser than the spatial projective field onto the SC. This implies that stimuli as large as 30° will be processed with some bias towards a certain contour orientation.

This unexpected result was scrutinized further. Intrinsic reflectance represents a bulk signal from the tissue, and the stimuli used to map orientation tuning and projective fields might excite two different sets of neurons. We therefore returned to two-photon calcium imaging to examine individual neurons. For each orientation-tuned neuron in several volumes we mapped the visual receptive field with small flashed spots (Fig. 5g). The receptive fields were comparable in size (median diameter, 10°; median area, 74°^{2}) to off-type receptive fields reported in anaesthetized mice[14]. Neurons were grouped by their preferred orientations into bins centred on 0, 45, 90 or 135°. The receptive field centres of cells preferring the same orientation were found clustered in visual space, separated from those preferring a different orientation (Fig. 5h). Moreover, there was little overlap between the receptive fields of cells preferring different orientations (Fig. 5h). Consistent with these observations, cells with a given orientation preference responded much more strongly to spots flashed in the consensus receptive field centre (Fig. 5h) of the cells sharing that preferred orientation (median 100%, mean 81%, fraction of peak response; 4 animals, 63 cells) than to the receptive field centre of cells with a different preferred orientation (median 29%, mean 38%; $P < 0.001$, Kruskal–Wallis test). Thus, both intrinsic imaging and two-photon calcium imaging reveal that adjacent orientation columns in the SC survey largely non-overlapping regions in space, in violation of position invariance and uniform coverage. These orientation patches cover large regions of the visual field (~30°) compared to the mouse's acuity (~2°)[20]. Furthermore, the absolute magnitude of this inhomogeneity is substantial. The average orientation-tuned neuron (OSI = 0.30) has a 2:1 bias in favour of the preferred orientation, so the relative gain for orthogonal orientations in adjacent patches may differ by a factor of 4. For regions of the visual field spanning several tens of degrees, the SC favours one orientation and responds less well to stimuli of other orientations (Fig. 5i).

It is not apparent how columnar architecture arises in the SC. Perhaps afferents from distinct retinal ganglion cell subtypes are routed to different orientation patches by different rules. Indeed, the terminal arbors of certain retinal ganglion cell types show a vertical columnar structure, albeit on a slightly finer scale[21,22]. Additional hints at non-uniform anatomy are the lattices formed deeper in the SC by cholinergic[23–25] and nigro-collicular[26] fibres, again on the scale of several hundred micrometres. The tuning field for contour orientation (Fig. 5i) may also relate to regional specializations in the SC. For example, stimulation of regions of the SC that survey the upper or lower visual field elicits avoidance or approach behaviours, respectively[27–29]. This subdivision seems coarser than the observed orientation tuning maps, and a more refined study of behaviours supported by the SC, along with further exploration of functional architecture in response to diverse stimuli[30] across the full retinotopic map, will help in understanding the functional significance of these columns in the SC.

Online Content Methods, along with any additional Extended Data display items and Source Data, are available in the online version of the paper; references unique to these sections appear only in the online paper.

Received 6 August; accepted 24 November 2014.
Published online 17 December 2014.

1. Masland, R. H. The neuronal organization of the retina. *Neuron* **76,** 266–280 (2012).
2. Dhande, O. S. & Huberman, A. D. Retinal ganglion cell maps in the brain: implications for visual processing. *Curr. Opin. Neurobiol.* **24,** 133–142 (2014).
3. Wässle, H. Parallel processing in the mammalian retina. *Nature Rev. Neurosci.* **5,** 747–757 (2004).
4. May, P. J. The mammalian superior colliculus: laminar structure and connections. *Prog. Brain Res.* **151,** 321–378 (2006).
5. Ohki, K., Chung, S., Ch'ng, Y. H., Kara, P. & Reid, R. C. Functional imaging with cellular resolution reveals precise micro-architecture in visual cortex. *Nature* **433,** 597–603 (2005).
6. Hubel, D. H. & Wiesel, T. N. Receptive fields and functional architecture of monkey striate cortex. *J. Physiol. (Lond.)* **195,** 215–243 (1968).
7. Blasdel, G. G. & Salama, G. Voltage-sensitive dyes reveal a modular organization in monkey striate cortex. *Nature* **321,** 579–585 (1986).
8. Grinvald, A., Lieke, E., Frostig, R. D., Gilbert, C. D. & Wiesel, T. N. Functional architecture of cortex revealed by optical imaging of intrinsic signals. *Nature* **324,** 361–364 (1986).
9. Harris, K. D. & Mrsic-Flogel, T. D. Cortical connectivity and sensory coding. *Nature* **503,** 51–58 (2013).
10. Chen, T. W. *et al.* Ultrasensitive fluorescent proteins for imaging neuronal activity. *Nature* **499,** 295–300 (2013).
11. Dräger, U. C. & Hubel, D. H. Topography of visual and somatosensory projections to mouse superior colliculus. *J. Neurophysiol.* **39,** 91–101 (1976).
12. Dräger, U. C. & Hubel, D. H. Physiology of visual cells in mouse superior colliculus and correlation with somatosensory and auditory input. *Nature* **253,** 203–204 (1975).
13. Wang, L. *et al.* Direction-specific disruption of subcortical visual behavior and receptive fields in mice lacking the β2 subunit of nicotinic acetylcholine receptor. *J. Neurosci.* **29,** 12909–12918 (2009).
14. Wang, L., Sarnaik, R., Rangarajan, K., Liu, X. & Cang, J. Visual receptive field properties of neurons in the superficial superior colliculus of the mouse. *J. Neurosci.* **30,** 16573–16584 (2010).
15. Zhao, X., Chen, H., Liu, X. & Cang, J. Orientation-selective responses in the mouse lateral geniculate nucleus. *J. Neurosci.* **33,** 12751–12763 (2013).
16. Andermann, M. L., Kerlin, A. M., Roumis, D. K., Glickfeld, L. L. & Reid, R. C. Functional specialization of mouse higher visual cortical areas. *Neuron* **72,** 1025–1039 (2011).
17. Swindale, N. V., Shoham, D., Grinvald, A., Bonhoeffer, T. & Hubener, M. Visual cortex maps are optimized for uniform coverage. *Nature Neurosci.* **3,** 822–826 (2000).
18. Bosking, W. H., Crowley, J. C. & Fitzpatrick, D. Spatial coding of position and orientation in primary visual cortex. *Nature Neurosci.* **5,** 874–882 (2002).
19. Yu, H., Farley, B. J., Jin, D. Z. & Sur, M. The coordinated mapping of visual space and response features in visual cortex. *Neuron* **47,** 267–280 (2005).
20. Prusky, G. T. & Douglas, R. M. Characterization of mouse cortical spatial vision. *Vision Res.* **44,** 3411–3418 (2004).
21. Huberman, A. D. *et al.* Genetic identification of an On-Off direction-selective retinal ganglion cell subtype reveals a layer-specific subcortical map of posterior motion. *Neuron* **62,** 327–334 (2009).
22. Hong, Y. K., Kim, I. J. & Sanes, J. R. Stereotyped axonal arbors of retinal ganglion cell subsets in the mouse superior colliculus. *J. Comp. Neurol.* **519,** 1691–1711 (2011).
23. Ramon-Moliner, E. Acetylthiocholinesterase distribution in the brain stem of the cat. *Ergeb. Anat. Entwicklungsgesch.* **46,** 7–53 (1972).
24. Graybiel, A. M. A stereometric pattern of distribution of acetylthiocholinesterase in the deep layers of the superior colliculus. *Nature* **272,** 539–541 (1978).
25. Chevalier, G. & Mana, S. Honeycomb-like structure of the intermediate layers of the rat superior colliculus, with additional observations in several other mammals: AChE patterning. *J. Comp. Neurol.* **419,** 137–153 (2000).
26. Mana, S. & Chevalier, G. The fine organization of nigro-collicular channels with additional observations of their relationships with acetylcholinesterase in the rat. *Neuroscience* **106,** 357–374 (2001).
27. Dean, P., Redgrave, P., Sahibzada, N. & Tsuji, K. Head and body movements produced by electrical stimulation of superior colliculus in rats: effects of interruption of crossed tectoreticulospinal pathway. *Neuroscience* **19,** 367–380 (1986).
28. Sahibzada, N., Dean, P. & Redgrave, P. Movements resembling orientation or avoidance elicited by electrical stimulation of the superior colliculus in rats. *J. Neurosci.* **6,** 723–733 (1986).
29. Dean, P., Mitchell, I. J. & Redgrave, P. Responses resembling defensive behaviour produced by microinjection of glutamate into superior colliculus of rats. *Neuroscience* **24,** 501–510 (1988).
30. Basole, A., White, L. E. & Fitzpatrick, D. Mapping multiple features in the population response of visual cortex. *Nature* **423,** 986–990 (2003).

Supplementary Information is available in the online version of the paper.

Acknowledgements We thank E. Soucy and J. Greenwood for assistance with instrumentation; M. Joesch, A. Krishnaswamy, D. Kostadinov, S. Pashkovski, A. Giessel, T. Dunn, G. Keller, P. Kaifosh, M. Amoroso, and H. Asari for software; M. Andermann, V. Bonin, and F. Engert for advice on microscope design; J. Cohen for headplate designs; D. Anderson, K. Blum, B. Ölveckzy, and J. Sanes for critical reading of the manuscript; and J. Sanes for providing laboratory space and support to E.H.F. E.H.F. was supported by NIH T32 NS007484 and a Howard Hughes Medical Institute-Helen Hay Whitney Foundation fellowship. Additional support was provided by an NIH grant to M.M.

Author Contributions E.H.F. designed the study, performed all experiments, interpreted results, and wrote the manuscript. M.M. helped design the study, interpret results, and write the manuscript.

Author Information Reprints and permissions information is available at www.nature.com/reprints. The authors declare no competing financial interests. Readers are welcome to comment on the online version of the paper. Correspondence and requests for materials should be addressed to M.M. (meister@caltech.edu) or E.H.F. (evan_feinberg@post.harvard.edu).

METHODS

Mice. Experiments were conducted on adult C57BL6/J mice of both sexes (ages 2–8 months, Jackson labs). All procedures were performed in accordance with institutional guidelines. Mice were first anaesthetized with ketamine, xylazine, and acepromazine (60 mg per kg, 7.5 mg per kg, and 3 mg per kg, respectively) and placed in a stereotaxic device with eyes covered with ophthalmic ointment. A custom head plate (titanium, 1 mm thickness, eMachineShop) was bonded to the skull (ESPE Adper Scotchbond, 3M), roughly centred on lambda, parallel to the long axis of the mouse and at a pitch of 15 ± 5°. In some mice, viral injections were made through a small burr hole drilled over the rostral tip of the SC (injection coordinates 0.2–0.4 mm caudal to interaural line, 0.3–0.7 mm lateral). A glass pipette (25–35 μm tip) loaded with a 2:1 mixture of AAV2/1.hSyn1.GCaMP6s.WPRE.SV40 (Penn Vector Core) and 20% mannitol in saline was advanced into the tissue and a hydraulic injector was used to inject 90–270 nl over several minutes. The pipette was left in place for 3 min before progressing to the next depth. Injections were made at three depths, typically 1.3, 1.15, and 1 mm below lambda. The pipette was then slowly removed and the hole overlaid with Kwik-Cast silicone elastomer (World Precision Instruments). Animals were given buprenorphine and carprofen (0.1 mg per kg, 5 mg per kg, respectively) for 48 h post-operatively.

Previous intrinsic signal imaging studies of the SC entailed ablation of the overlying visual cortex (VC)[31,32]. This procedure destroys strong reciprocal connections between the SC and VC that likely influence response tuning, a potentially serious caveat. We noticed that the posteromedial SC is not obscured by cortex and might be accessible for imaging without removal of VC. This wedge of the SC lies beneath the confluence of the superior sagittal and transverse sinuses (Fig. 1a)[33]. Blood absorbs infrared and visible light, and these vessels form an opaque barrier that stymied initial imaging attempts. Ablation of the transverse sinus in humans with arteriovenous malformations typically causes minimal or no neurological symptoms[34], indicating that it is not essential for healthy brain function. Moreover, its location within the dura and consequent lack of physical attachment to the brain surface suggested the possibility of dislodging it without damaging the underlying SC. Several previous studies used 'plugs' of glass or transparent silicone to apply pressure normal to the brain surface to flatten the tissue and minimize motion artefacts[16,35]; we reasoned that triangular plugs could be used to apply pressure parallel to the brain surface, in a fashion analogous to a snowplow, to anteriorly displace the transverse sinuses (Fig. 1b, c and Extended Data Fig. 1a–c). With this approach, we were able to implant acute or chronic imaging windows and expose triangular patches of the SC typically 800–1,000 μm on a side, corresponding to ~15–25% of the surface area of the SC. We have successfully imaged the SC with this preparation from 30 min to 6 months after plug implantation.

Five days to 3 months after implantation of head plates, mice were given dexamethasone (2 mg per kg), anaesthetized with isoflurane, and immobilized via their head plates in a custom holder. In mice previously injected with AAV, a 2–3 mm craniotomy was made over the SC, inferior colliculus, and part of the cerebellum, and a large flap was opened in the dura with a 30-gauge needle. The tissue was kept moist under artificial cerebrospinal fluid (ACSF). ACSF was wicked from the craniotomy to leave only a thin film of liquid over the SC and a small drop of uncured Kwik-Sil was applied to the SC. A plug bonded to a 5 mm circular coverslip was mounted on a suction cup and positioned over the craniotomy. The plug was quickly advanced downward into the uncured drop of silicone and then anteriorly to displace the dura and transverse sinuses. Cyanoacrylate (Vetbond, 3M) was applied to bond the coverslip to the skull and headplate. After a few minutes, suction was released and the suction cup withdrawn. Black dental cement (Ortho-Jet, Lang Dental) was then applied over the cyanoacrylate on the skull, head plate, and edges of the cranial window and allowed to set for ~30 min. For mice that had not been injected with AAV, a similar craniotomy was performed over the SC as well as VC, virus was injected into the SC and VC as previously described, and a plug attached to an 8 mm coverslip was implanted as above.

To aspirate cortex, a craniotomy was performed over the SC and VC. Cortex was slowly aspirated and the transverse sinus was severed and reflected. Once bleeding had ceased, the craniotomy was filled with uncured Kwik-Sil and a coverslip was pressed in place above and bonded as previously described.

At least 3 days after implanting cranial windows, mice were habituated to handling and head-fixing for at least 3 days before experiments began; mice were given at least 7 days after injection to permit GCaMP expression, and indistinguishable results were obtained 7 days to 3 months after AAV injection. Mice were head-fixed on a 12 cm diameter circular treadmill (Ware Flying Saucer). The underside of the wheel was painted with alternating stripes of black and silver and illuminated with 940 nm light-emitting diodes (LEDs). A pair of photodiodes measured reflectance of the stripes and thus encoded wheel motion for steps >5 mm. Analogue signals were recorded and analysed in Matlab.

Plugs. Uncured Kwik-Sil (World Precision Instruments) was pressed between two ~2.5 cm square blocks of acrylic (previously sterilized with 70% ethanol) separated by 0.75 mm shim stock. The silicone was allowed to cure for at least 15 min and transferred to a sterile Petri dish. A scalpel was used to cut triangular prisms roughly 1 mm tall and 1.5 mm wide. Care was taken to avoid use of any portion of the silicone sheet containing bubbles or lint. Surfaces of the silicone plugs were cleaned with transparent adhesive tape to remove dust. A corona treater (Electrotechnic products) was used to activate the surfaces of a silicone plug and a coverslip (5 or 8 mm, number 1 thickness, Warner) and the plug was placed on the coverslip with the activated surfaces touching. Plugs were placed in a sterile Petri dish and bonding was allowed to proceed overnight in a hybridization oven at 60–70 °C. To implant plugs, small suction cups were fabricated by bevelling a 25-gauge needle to ~45° and mounting the needle with the aperture facing downward on a micromanipulator with a 20 ml syringe attached through flexible tubing. A small drop (~1 mm diameter) of ACSF was set on a clean block of acrylic and the tip of the syringe was placed in the drop. Kwik-sil was applied over the tip and allowed to set for at least 15 min before use.

Two-photon microscope. Two-photon imaging was performed on a custom-built microscope controlled by software written in Labview (National Instruments). A mode-locked Ti:sapphire laser (Mai-Tai DeepSee, Newport) with group delay dispersion compensation was scanned by galvanometers (Cambridge) through a 20× 1 NA water-immersion objective (Olympus). GCaMP6s was excited at 920 nm and laser power at the sample plane was typically 15–50 mW. Imaging in the SC was performed 50 μm to 300 μm below the surface, and imaging in layer 2/3 of VC was performed 150 μm to 300 μm below the surface. A 300 × 150 μm field of view was scanned at 8 Hz as a series of 300 × 150 pixel images. Emitted light was collected with a T600/200dcrb dichroic (Chroma) and a 610dxcr dichroic (Chroma) to split green and red light (no red fluorophore was used in this study); green light passed through a HQ600/200M-2P bandpass filter (Chroma) and was detected by a multialkali photomultiplier tube (R3896, Hamamatsu). Artefacts of the strobed stimulus were eliminated by discarding 10 pixels on either end of each line to yield 280 × 150 pixel images.

Intrinsic imaging microscope. Reflectance of a 735 nm LED (Thorlabs) was collected using a CCD camera (Flea3, Point Grey), through a 5× 0.14 NA air objective (Mitutoyo) used as a 2.5× objective with a short (f = 100 mm) tube lens. Images of 640 × 480 pixels at 8-bit resolution were acquired at 114 or 120 Hz and binned to 6 Hz, 160 × 120 pixels. Acquisition and analysis used custom software written in Labview and Matlab (Mathworks).

Visual stimuli. Stimuli were generated in Psychtoolbox3 (Matlab) and presented on an LCD screen (Dell, U2312HM) centred 23 cm away from the mouse's eye, angled at 20° in pitch and yaw to minimize fisheye distortion. Stimuli were presented on a square (1,080 × 1,080 pixel) region of the screen. Between experiments the monitor was maintained at a constant background grey level. To minimize interference of the stimulus with fluorescence detection, the monitor was strobed for 2 μs at the end of each scan line (1,200 Hz; luminance of grey screen ~1.25 cd m^{-2}, maximum brightness ~1/80 of unmodified monitor). Mice see red poorly, and all stimuli presented used only the green and blue channels of the monitor. The red channel was used to convey stimulus timing to synchronize with fluorescence acquisition; red bars flickered periodically at the bottom of the screen, which was covered with black tape. Drifting bars were 40 pixels wide (2–3°) and drifted at a speed of 240 pixels per s (12–18° s^{-1}). Flashed spots were presented as a 10 × 10 grid of 5–8° black squares. Each spot appeared for 500 ms and was followed by 500 ms of grey screen. All stimuli in two-photon experiments were presented in a pseudorandom sequence with interspersed blank periods (sampling with replacement) within each stimulus block (typically 6–8 blocks per experiment), with a different random seed for each block.

For intrinsic imaging, the same monitor was used. Due to the larger number of repetitions required, in some experiments the drifting bar stimuli were presented with interspersed blank frames omitted. To map the projective fields of slit gratings, a square wave grating with 100% contrast, spatial frequency of 0.5–0.8 cycles per degree (cpd), and temporal frequency of 1 Hz, switching direction after each cycle, was presented for 8 s through an aperture of the same dimensions as the drifting bars. To map the projective fields of grating patches, the same square grating was presented through a square aperture (10–15°) that alternated between two abutting locations every 8 s, changing to a randomly chosen (with replacement) cardinal direction every 1 s.

Calcium imaging analysis. Brain motion during imaging was corrected using TurboReg (ImageJ) or software written in Python[36]. Elliptical regions of interest (ROIs) were drawn manually in Matlab and fluorescence traces extracted and neuropil signals subtracted. Neuropil tended to share the orientation tuning of the embedded cells (Extended Data Fig. 5). Because much of the neuropil derives from processes of the local cells, if local cells are tuned alike, the surrounding neuropil will show similar tuning, as in orientation columns in cat visual cortex[5,37]. Thus, this observation was consistent with the single-cell data, but also presented a potential experimental confound, because out-of-focus fluorescence from neuropil leaks into

the signals recorded from individual cells[38,39] (Extended Data Fig. 5b), and contamination by a tuned neuropil signal could bias measurements of a cell's true preferred orientation. The true fluorescence signal of a neuron is $c = r - (f \times n)$, with r the raw fluorescence signal of the ROI containing the cell, f the out-of-focus neuropil contamination factor, and n the fluorescence signal of the surrounding neuropil. To estimate the extent of this contamination, small non-vertical blood vessels were identified, as in previous studies[39], and cell-sized 'holes' that likely corresponded to uninfected cells. The ratio of their brightness and that of the surrounding neuropil was measured, and this routinely yielded estimates of $f = \sim 0.5$, a value similar to that obtained by another group using an objective with NA 1 (ref. 39). As a result, all data presented in this study were processed using this value of f. A shell of radius 20 μm centred on each cell was taken from the masked image, excluding all cells, and used to calculate the corrected signal for neuropil contamination. Cells with bright, filled nuclei, known to have slower kinetics and/or aberrant responses[40], were excluded from analysis but included in masks for neuropil subtraction[10,40]. Nevertheless, the true value of f may vary slightly within a field of view, and to ensure that the central results were robust to this variation we repeated the analysis with values of f from 0.3 to 0.9. For each value of f in this range, neurons were much more similar to the surrounding neuropil and each other than chance (Extended Data Fig. 5c, d), confirming that cells are indeed tuned similarly to their neighbours and the surrounding neuropil.

On occasion, frames with large-amplitude motion were not registered correctly. These frames can be easily identified because activity should cause only increases in the fluorescence signal for an ROI, while movement of a cell into or out of an ROI is likely to be associated with either increases or decreases in fluorescence[35]. To detect these events, we estimated the baseline fluorescence for each ROI as the mean of the lower half of its fluorescence intensity over the course of the movie, and discarded frames in which the fluorescence of any ROI was more than 3 s.d. below baseline. Slow baseline fluctuations were removed by subtracting the eighth percentile value from a moving window 15 s wide centred on each frame[35]; the mean value of the eighth percentile value for the entire trace was then added back to allow measurement of fold changes. The response to each direction ($\Delta F/F$) was measured as $(F/F_0)-1$, with F the instantaneous ROI intensity and F_0 the mean fluorescence intensity during stimulus blanks (grey screen). $\Delta F/F$ values for each presentation of a stimulus were averaged and the peak $\Delta F/F$ for each direction was used to compute orientation preference; similar results were obtained using the mean $\Delta F/F$ for each ROI. Responses to directions separated by 180° were summed to compute orientation preference. The orientation selectivity index (OSI) was calculated as $(R_{\mathrm{pref}} - R_{\mathrm{ortho}})/(R_{\mathrm{pref}} + R_{\mathrm{ortho}})$, with R_{pref} the $\Delta F/F$ to the orientation eliciting the strongest response and R_{ortho} the $\Delta F/F$ to the orthogonal orientation[15]. Cells with OSI ≥ 0.15 (~4:3 preferred:null response) were classified as orientation-selective. The preferred orientation was defined as the weighted vector sum over the range of presented stimulus angles.

To map receptive fields with flashed spots, stimuli were presented in rapid succession, necessitating a faster baseline filter (3 s) to compensate for the slow decay kinetics of the GCaMP6s. The consensus centre square for each field of view, averaging all cell bodies and neuropil, was identified and the mean responses to spots on the periphery, well outside the receptive fields, and blanks were averaged to compute baseline fluorescence F_0 for each ROI. The response $\Delta F/F$ was computed as $(F/F_0)-1$, with F representing the peak of the averaged response of all presentations for each spot location. To compare receptive field overlap, preferred orientation for each cell was binned to 0, 45, 90, or 135°, according to the presented orientation eliciting the strongest response. Next, the number of cells preferring each orientation was determined, and the orientations preferred by the largest fraction of cells (orientation 1) and second-largest fraction of cells (orientation 2) were analysed. The peak square location for each cell preferring orientation 1 or orientation 2 was defined as the location that elicited the maximal responses from the plurality of cells sharing each preferred orientation. A two-dimensional Gaussian was fit to each orientation-tuned cell's responses to the flashed spots and the receptive field size was set as the area of an ellipse of radius of one s.d., using a spot area of 7.5°.

Intrinsic imaging analysis. No temporal or spatial filtering of intrinsic imaging data was performed. To map orientation columns, mean reflectance changes while bars drifted in both directions were summed for each cardinal axis. An ROI was drawn manually over the SC to exclude signals from the large surrounding blood vessels, and the ratio of responses to the vertical and horizontal axes was determined. To measure the projective fields of slit gratings, the ratio of the mean reflectance to a given grating position was taken to the mean reflectance when orthogonal bars were presented across the SC. To map projective fields with grating patches, the ratio of the mean reflectance when the stimulus was at either of the two locations was determined. Measurements of projective field peak-to-peak distances were made in ImageJ by drawing a rectangular ROI over each projective field, roughly orthogonal to the bar, and measuring the averaged line profile over the ROI. These line profiles were smoothed and full-width at half-maximum was measured in Matlab. To measure inhomogeneity indices, pixels were classified as preferring horizontal or vertical if they were in the upper 40% of responses to either orientation, with the remaining pixels classified as untuned. A window of indicated size was rastered across the orientation map. At any position in which more than half of the pixels were within the SC mask, the inhomogeneity index was measured as, $abs\ (h - v)/(h + v + u)$ with h and v the number of pixels preferring horizontal and vertical bars, respectively, and u the number of untuned pixels. To generate the image in Fig. 5i, lines were manually fit to the projections of slit gratings (as in Fig. 5a–c) on the surface of the SC. The resulting grid was then aligned to a grid of the positions of the stimuli in the visual field using a thin plate spline in Matlab, and the same transform applied to the orientation map from that animal.

Statistical methods. No statistical method was used to predetermine sample size. Statistical comparisons were performed as Kruskal–Wallis tests, a non-parametric test that extends the Mann–Whitney U-test to multiple groups, or as Monte Carlo simulations. These tests do not assume normality of the data; nevertheless, all comparisons described yielded similar P values with statistical methods that assume normality (for example, one-way ANOVA).

31. Mrsic-Flogel, T. D. *et al.* Altered map of visual space in the superior colliculus of mice lacking early retinal waves. *J. Neurosci.* **25,** 6921–6928 (2005).
32. Cang, J., Wang, L., Stryker, M. P. & Feldheim, D. A. Roles of ephrin-as and structured activity in the development of functional maps in the superior colliculus. *J. Neurosci.* **28,** 11015–11023 (2008).
33. Dorr, A., Sled, J. G. & Kabani, N. Three-dimensional cerebral vasculature of the CBA mouse brain: a magnetic resonance imaging and micro computed tomography study. *Neuroimage* **35,** 1409–1423 (2007).
34. Wong, G. K., Poon, W. S., Yu, S. C. & Zhu, C. X. Transvenous embolization for dural transverse sinus fistulas with occluded sigmoid sinus. *Acta Neurochirurgica* **149,** 929–935 (2007).
35. Dombeck, D. A., Khabbaz, A. N., Collman, F., Adelman, T. L. & Tank, D. W. Imaging large-scale neural activity with cellular resolution in awake, mobile mice. *Neuron* **56,** 43–57 (2007).
36. Kaifosh, P., Lovett-Barron, M., Turi, G. F., Reardon, T. R. & Losonczy, A. Septo-hippocampal GABAergic signaling across multiple modalities in awake mice. *Nature Neurosci.* **16,** 1182–1184 (2013).
37. Ohki, K. & Reid, R. C. *In vivo* two-photon calcium imaging in the visual system. *Cold Spring Harb. Protoc.* **2014,** 402–416 (2014).
38. Göbel, W. & Helmchen, F. *In vivo* calcium imaging of neural network function. *Physiology* **22,** 358–365 (2007).
39. Kerlin, A. M., Andermann, M. L., Berezovskii, V. K. & Reid, R. C. Broadly tuned response properties of diverse inhibitory neuron subtypes in mouse visual cortex. *Neuron* **67,** 858–871 (2010).
40. Tian, L. *et al.* Imaging neural activity in worms, flies and mice with improved GCaMP calcium indicators. *Nature Methods* **6,** 875–881 (2009).

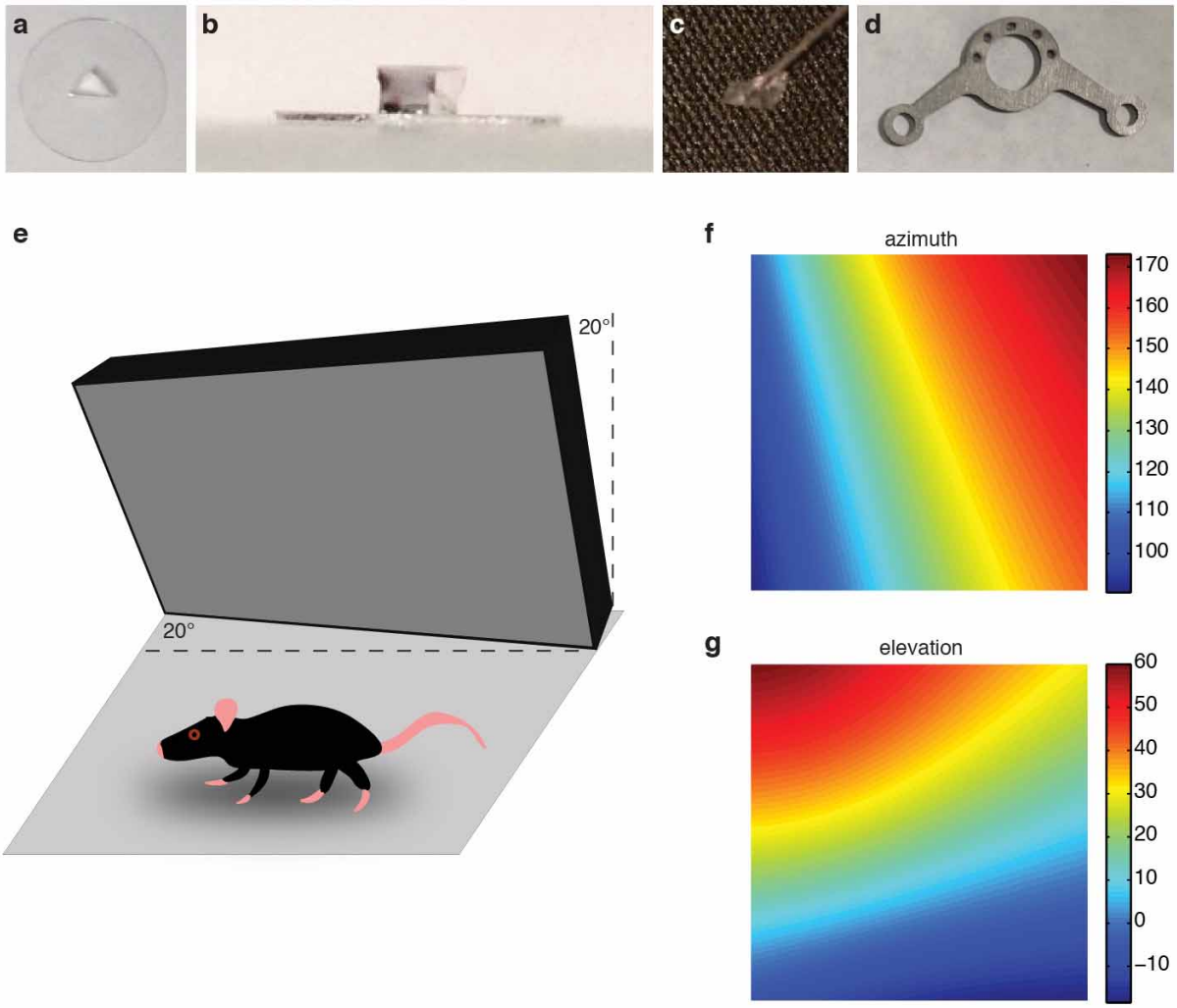

Extended Data Figure 1 | Plugs and head plates used for this study. **a**, Top view of triangular silicone plug attached to a 5 mm coverslip. **b**, Side view of the plug from **a**. **c**, Suction cup used to position plug. **d**, Standard headplate with 8 mm aperture. **e**, Monitor tilt used to reduce fisheye distortion. Perspective is exaggerated for clarity. The monitor was tilted such that it was 20° from vertical, with the top nearer the animal, and 20° from the animal's anterior–posterior axis, with the right edge closer to the animal. Note that stimuli were presented in a square area on the right side of the rectangular monitor. **f**, **g**, Azimuth and elevation in degrees for each pixel within the inscribed square area of the monitor on which stimuli were displayed. Values are given with respect to standard stereotaxic coordinates; because headplates were implanted at ~15° angles with respect to this plane, bars on screen are tilted. Curvature of elevation bars reflects the fact that iso-elevation lines are curved, not straight, much like latitude lines on a globe.

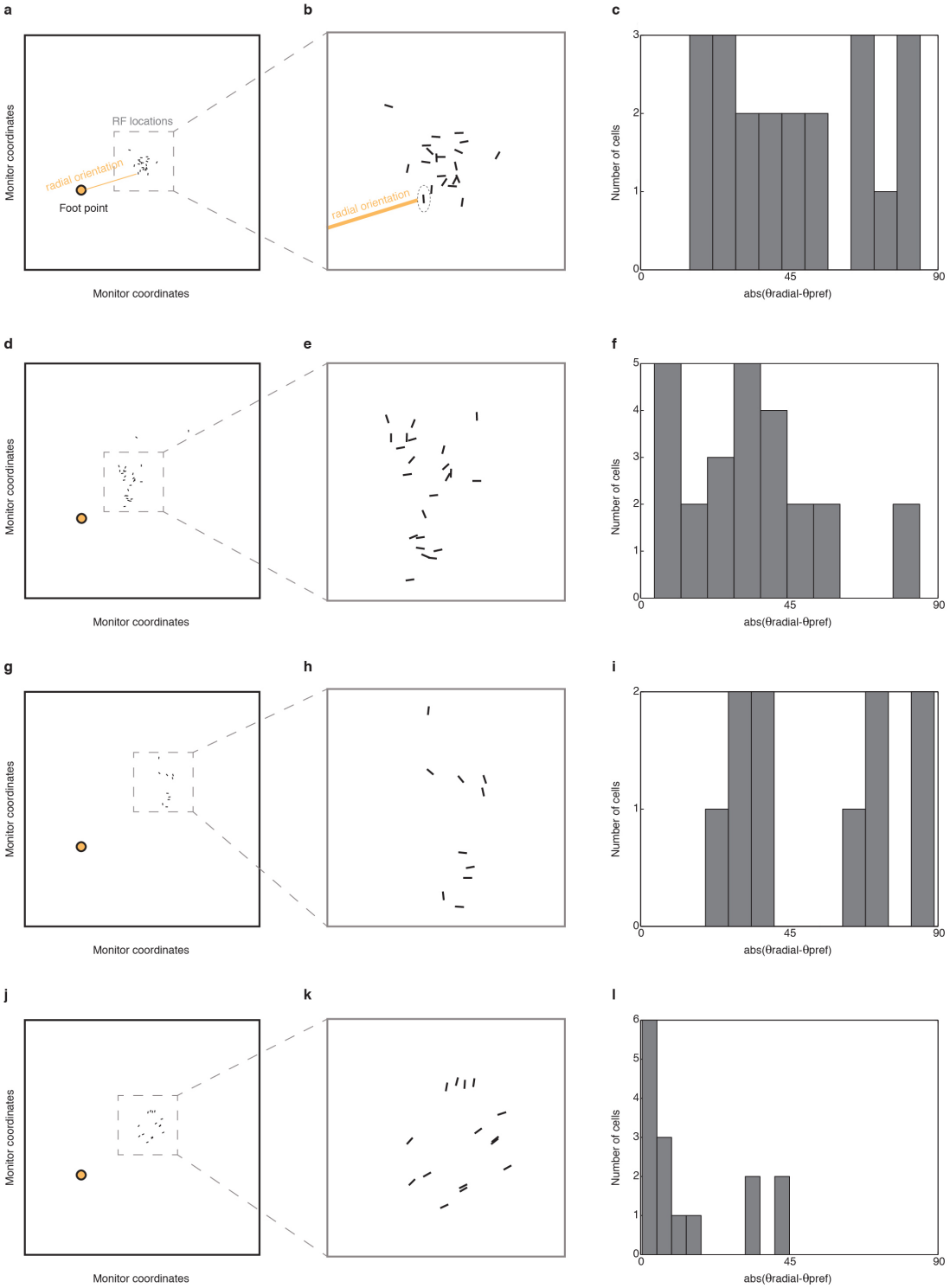

Extended Data Figure 2 | Orientation tuning does not reflect distortion effects of flat screen. **a**, Plot of foot point of monitor (FP), the point at which a line from the eye is perpendicular to the tangent screen, and all mapped receptive field centres for orientation-tuned SC neurons in one animal. Each line segment is positioned at a cell's receptive field centre and angled to reflect its preferred orientation. Orange line indicates the radial orientation relative to the FP for an example cell. Fisheye distortion will cause bars along the radial orientation relative to the foot point to appear relatively wider and faster than orthogonal bars along the tangential orientation, potentially biasing responses towards or away from the radial orientation. **b**, Enlarged view of inset area in **a** to show orientations more clearly. Note sharp transition in preferred orientation from bottom to top of panel relative to difference in radial orientation. Also note that the preferred orientation and the radial orientation vary with opposite handedness. **c**, Difference between radial orientation and preferred orientation for all cells in the plot. If the orientation map were due to fisheye distortion, preferred orientations should be similar to the radial orientation and the distribution should be centred at 0. Note that this distribution is biased away from 0 and centred between 45 and 90°. **d**–**f**, As in **a**–**c** for another animal. Note sharp transition in preferred orientations as in **b**, but with opposite handedness, and centring of distribution of preferred orientations between 0 and 45°. **g**–**i**, As in **a**–**c** for another animal. Note sharp transition in preferred orientations and bias of cells to orientations orthogonal to radial orientation. **j**–**l**, As in **a**–**c** for another animal. Note sharp transition in this field and a group of cells whose preferred orientations are close to radial.

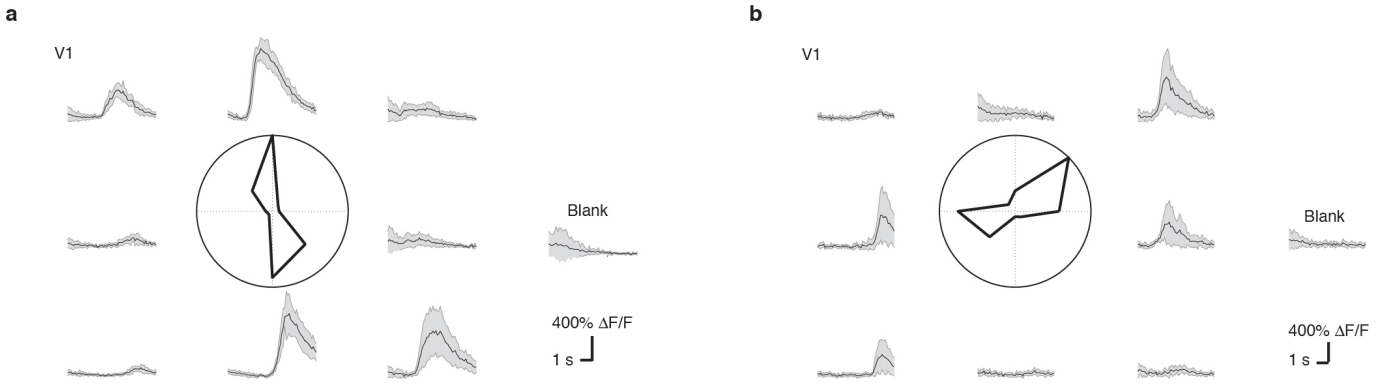

Extended Data Figure 3 | Sample responses of neurons in V1. a, **b**, Average $\Delta F/F \pm$ s.d. of two V1 neurons to 7 repetitions each of 8 directions of bar motion and a blank screen. Insets are polar plots for each cell.

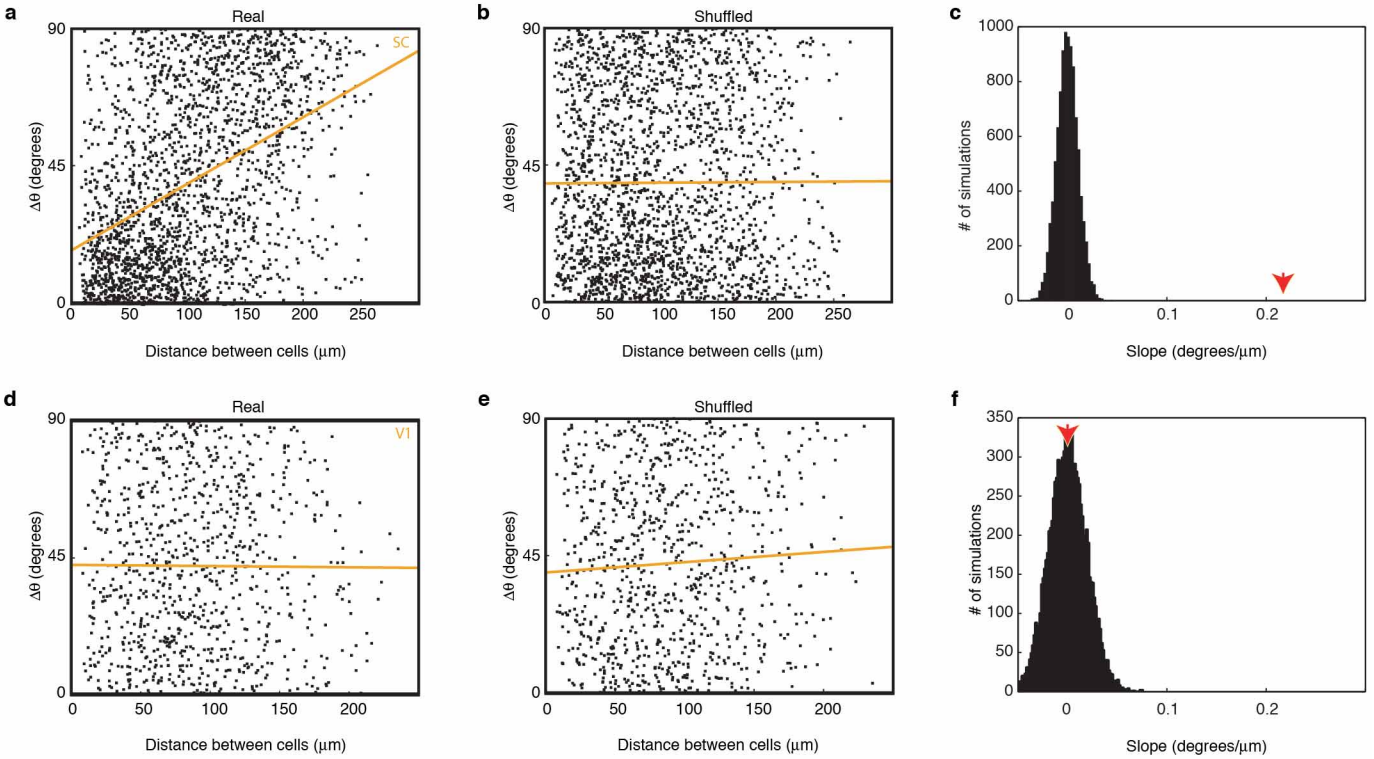

Extended Data Figure 4 | Monte Carlo simulation reveals significance of observed local similarity in the SC. **a**, Absolute value of the difference in preferred orientations plotted against horizontal distance in the SC. Orange line indicates linear fit to the difference in preferred orientation as a function of horizontal separation, yielding a line of best fit with a slope of $+22^\circ$ per 100 μm. **b**, As in **a** after shuffling all cell positions. A total of 10^5 independent shuffles were performed; shown are results from the final shuffle. This yielded a distribution of slopes with a mean ± s.d. of ($0 \pm 1^\circ$) per 100 μm. **c**, Histogram of slopes of best-fit lines from 10^5 independent Monte Carlo simulations. Arrowhead indicates slope from **a**. **d**–**f**, As in **a**–**c** for data from V1.

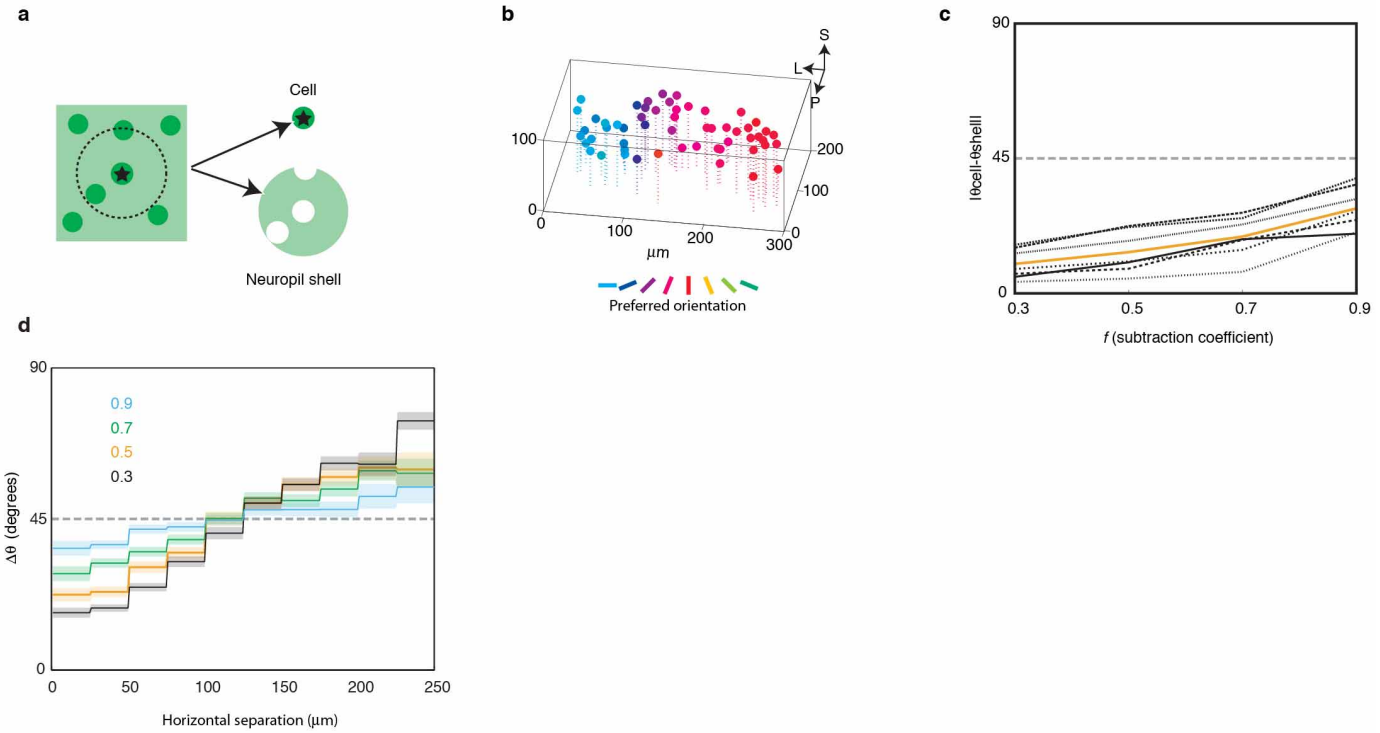

Extended Data Figure 5 | Orientation tuning of neuropil. **a**, Schematic of cells and surrounding neuropil shell. Signals are extracted from each cell and from the neuropil within 20 µm. The corrected signal of a cell c within an ROI r is $c = r - (f \times n)$, with n the signal of the neuropil shell and f the fractional contamination by out-of-focus neuropil. **b**, Orientation preferences for neuropil shells of orientation-tuned cells in Fig. 2a. **c**, Difference in preferred orientation of neurons and their neuropil shells over a range of values of neuropil subtraction coefficient f. Dashed horizontal line indicates chance. Each black line reflects median values from a single image volume; orange line is median value for all cells from 7 volumes. **d**, Effects are robust over a range of f values. Plotted are mean differences in preferred orientations against distance ± s.e.m as in Fig. 2d, from which the orange trace is reproduced. Because the neuropil is also sharply tuned, using high values of f will reduce the apparent similarity of neighbouring cells' orientation preferences. Nonetheless the similarity remains significant even at the excessively high f value of 0.9.

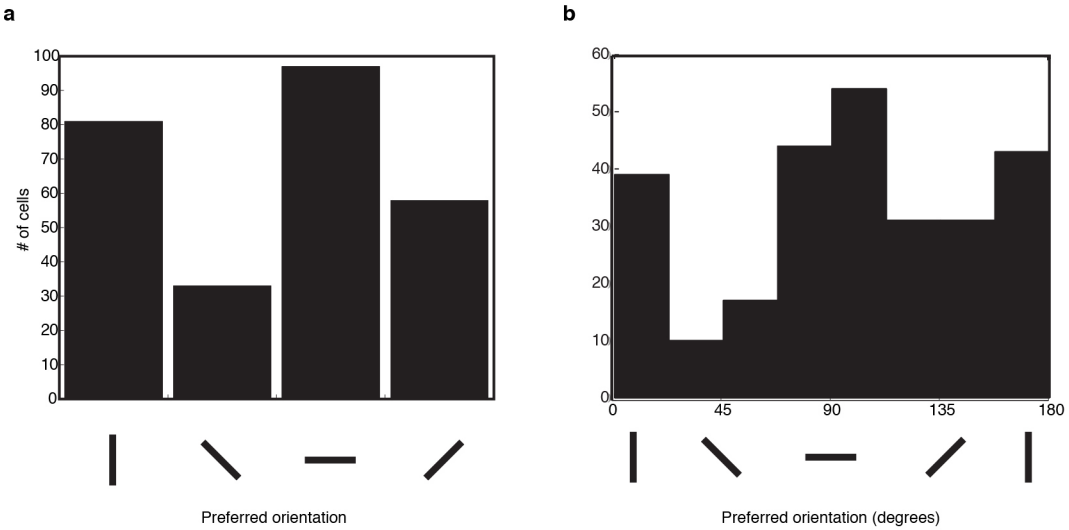

Extended Data Figure 6 | Distribution of preferred orientations in the SC. **a**, Preferred orientations of cells in the SC according to the presented orientation eliciting the strongest response. **b**, Preferred orientations of cells in the SC calculated from vector sums of responses to all orientations.

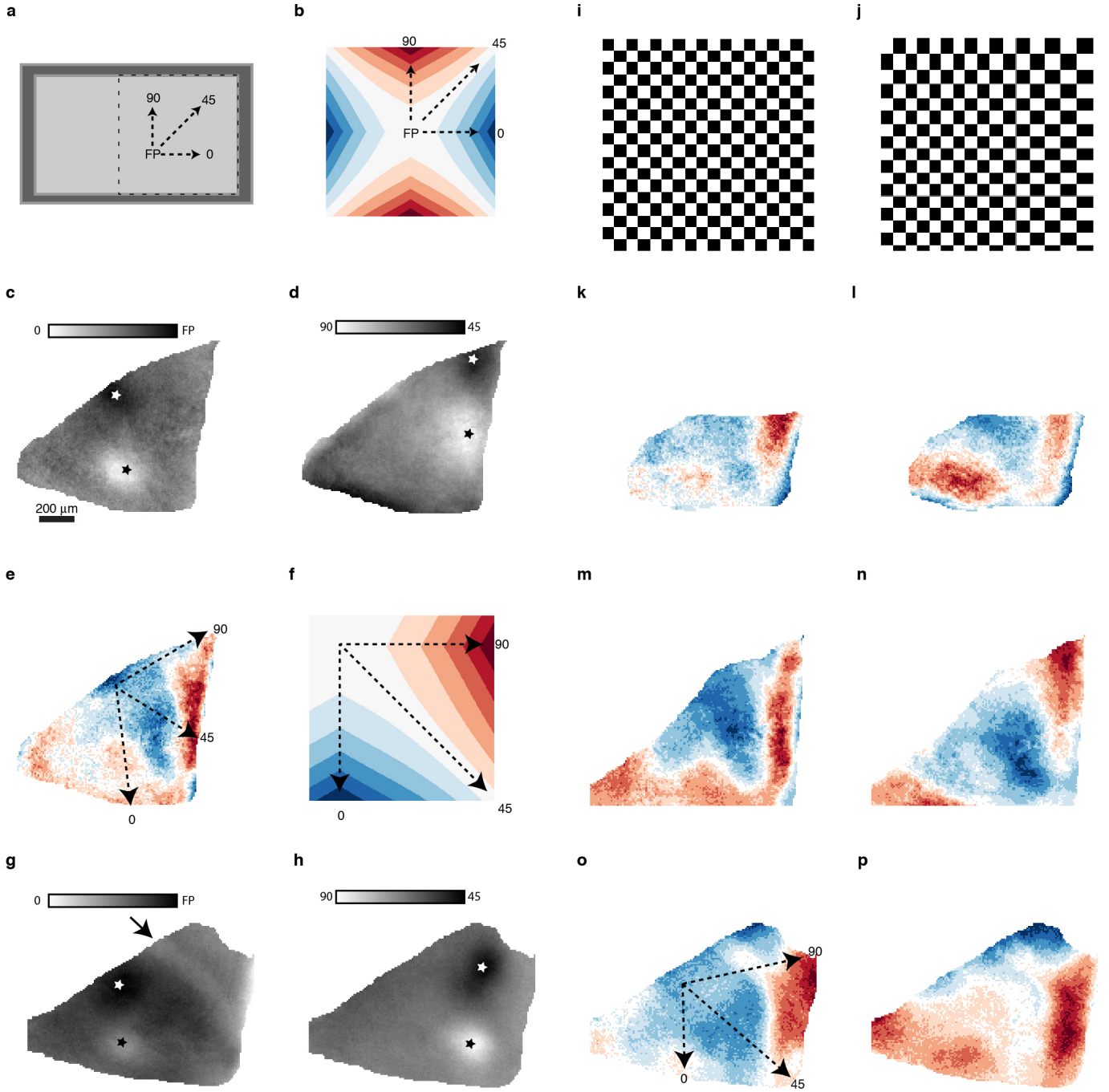

Extended Data Figure 7 | Orientation maps do not reflect fisheye distortion. **a**, Grating patches were presented at the foot point (FP), the point at which a line from the eye is perpendicular to the tangent screen, and at locations on the screen displaced from the FP along radial orientations of 0, 45, and 90°. **b**, Predicted map if fisheye distortion caused orientation tuning to be biased towards the radial orientation with respect to the FP. **c**, Projective field of foot point (black, indicated with white star) and patch at 0° (directly lateral on screen) from foot point (white patch, black star). **d**, As in **c** for patches at 90 and 45° with respect to foot point. **e**, Orientation map for this animal. Blue areas prefer horizontal bars, red areas prefer vertical bars, and arrows indicate lines from projective field of foot point to projective fields of patches. **f**, Expected orientation map according to distortion hypothesis. Note that the area at the projective field of the foot point should be untuned, and a line from the projective fields of the FP and a spot located at 0° relative elevation should pass from untuned areas to progressively more horizontal-preferring areas. Instead, it passes from a horizontal-preferring area at the FP to vertical-preferring areas as it moves to greater eccentricity. Trajectories along other projections of radial orientations (45 and 90°) are similarly poor fits to prediction. **g**, **h**, As in **b** and **c** for another animal. Orientation map for this animal in **o** also does not match prediction of fisheye distortion hypothesis. Arrow indicates shadow of blood vessel. **i**, **j**, Checkerboard pattern before and after 'pre-distortion' to offset fisheye effect. This pre-distortion was applied to change bar width by 1/cosine(θ), with θ the eccentricity from the FP, for both vertical and horizontal bar stimuli. **k**, **l**, Orientation maps for an animal in response to standard (**k**) and 'pre-distorted' (**l**) bar stimuli. In this animal the transverse sinus was not fully retracted and partially obscures the field of view. Note similarity of patterns in **k** and **l**. **m**, **n**, As in **k**, **l**, for the animal in **c**–**e** imaged on a different day. Comparison of maps in **e** and **m** reveals inter-trial variability, which is comparable to variability between standard and pre-distorted stimuli (**m** and **n**). **o**, **p**, As in **k**, **l** for a third animal. Map in **o** is overlaid with projective fields of points in visual field as in **e**. The reflectance change $\Delta R/R$ from black to white is 12×10^{-4} (**c**), 19×10^{-4} (**d**), and 18×10^{-4} (**g**, **h**). The reflectance change $\Delta R/R$ from red to blue is 4×10^{-4} (**e**, **k**, **o**), 5×10^{-4} (**l**, **p**), 7×10^{-4} (**m**), and 9×10^{-4} (**n**).

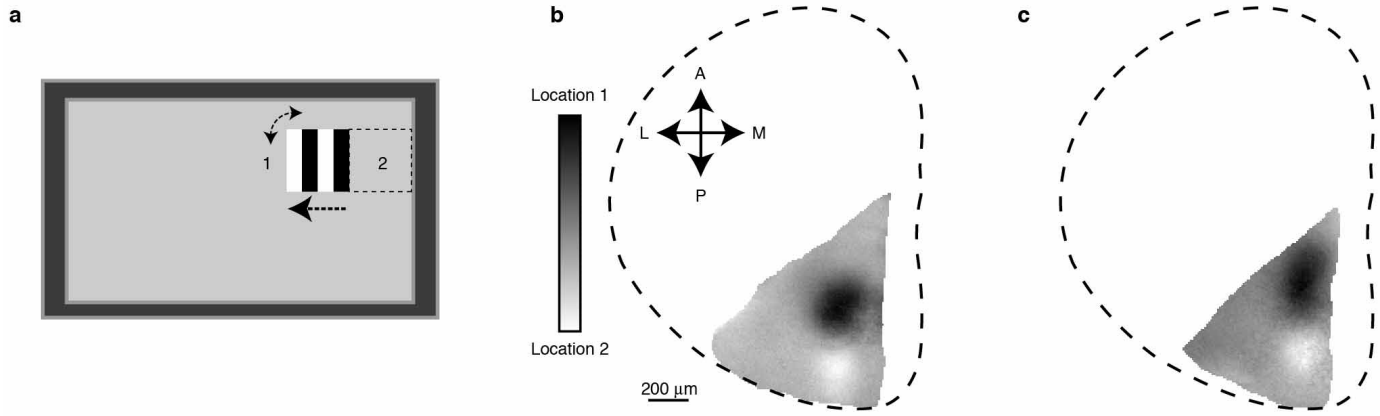

Extended Data Figure 8 | Alternative mapping stimulus reveals similar projective fields. **a**, Stimulus. Square grating patches alternate between two adjacent locations every 8 s. At each location the grating switches orientation randomly at 1 Hz. **b**, Map of responses elicited in animal from Fig. 4a. Responses to the two gratings span small patches on the surface of the SC. The reflectance change $\Delta R/R$ from black to white is 2×10^{-3}. **c**, As in **b** for animal from Fig. 4c. The reflectance change $\Delta R/R$ from black to white is 2×10^{-3}.